Quantum localization in the three-dimensional kicked Rydberg atom

Emil Persson,[1] Shuhei Yoshida,[1] Xiao-Min Tong,[2] Carlos O. Reinhold,[3] and Joachim Burgdörfer[1]
[1]*Institute for Theoretical Physics, Vienna University of Technology, A 1040 Vienna, Austria*
[2]*Kansas State University, Manhattan, Kansas 66506, USA*
[3]*Physics Division, Oak Ridge National Laboratory, Oak Ridge, Tennessee 37831-6372, USA*
(Received 25 March 2003; published 11 December 2003)

We study the three-dimensional (3D) unidirectionally kicked Rydberg atom. For parabolic initial states elongated in the direction of the kicks we show that the ionization of the quantum system is suppressed as compared to the classical counterpart and that the quantum wave function is localized along all degrees of freedom, whereas the classical system is globally diffusive. We discuss the connection to the previously studied one-dimensional (1D) model of the kicked Rydberg atom and verify that the 1D model is a good approximation to the 3D quantum case in the limiting case of the most elongated initial states. We further study the quantum phase-space distribution (Husimi distribution) of the eigenstates of the period-one time-evolution (Floquet) operator and show that the eigenstates are localized in phase space. For the most elongated parabolic initial state, we are able to identify the unstable periodic orbits around which Floquet states localize. We discuss the possibility of observing quantum localization in high Rydberg states in $n>100$.

DOI: 10.1103/PhysRevA.68.063406 PACS number(s): 32.80.Rm, 05.45.Mt, 32.60.+i

I. INTRODUCTION

The classical-quantum correspondence in the long-time evolution of classically chaotic few degrees of freedom systems has become one of the intensively investigated issues in the field of ''quantum chaos'' [1–3], i.e., the quantum dynamics of classically chaotic systems. One key feature is termed ''quantum localization,'' i.e., the localization of the wave function while the corresponding classical distribution shows diffusion [2,3]. Primarily two model systems have provided considerable insights into this phenomenon: the periodically kicked rotor [4–8] and the Rydberg atom in a harmonic electric driving field [3,9–15]. Recently, a third model system has become experimentally accessible [16–18], the ''kicked'' Rydberg atom, that is, the hydrogen atom perturbed by a periodic sequence of ultrashort unidirectional pulses. The experimental study of this previously theoretically investigated system [19–24] generated a large number of investigations, see, e.g., Refs. [25–30]. One common feature of these periodic systems is the discordance between quantum and classical dynamics [31] when the classical dynamics is strongly diffusive. The quantum suppression of diffusive motion in classical phase space for finite $\hbar$ is caused by a variety of mechanisms, only some of which are well understood. For the kicked rotor, it could be shown that a one-to-one mapping onto the Anderson localization problem [5,32,33] in disordered solids exists. Localization has also been extensively analyzed for the microwave driven Rydberg atom [3,10–15]. In this case, different localization mechanisms have been identified, such as Anderson localization [11], ''scarring'' of the Floquet states by unstable periodic orbits [12–14], and suppression of quantum phase flow by cantori [34], i.e., broken tori.

Recently we found first evidence of quantum localization for the unidirectionally and periodically kicked Rydberg atoms by studying a one-dimensional (1D) model [35]. The present system differs from previously studied ones in several aspects. The main difference between the kicked Rydberg atom and the kicked rotor is the presence of a continuum of the unperturbed atomic system, leading to the possibility of decay of the system. On the other hand, the main differences to the harmonically driven atom are the presence of higher harmonics in the periodic perturbation, which prevents a direct mapping onto a photonic localization description [3,12], and the unidirectionality of the field leading to a preferred direction in space. Moreover, the experimental studies of the periodically kicked Rydberg atom have been performed at much higher principal quantum number ($n \gtrsim 350$), i.e., much further into the (semi) classical regime. Both experimental and theoretical observation of quantum effects such as localization or revival in such a system remains a challenge.

The aim of the present paper is the identification of quantum localization in the three-dimensional (3D) kicked Rydberg atom and the investigation of the prospect of its experimental verification. Classical simulations within the framework of the classical-trajectory Monte Carlo method have proven remarkably successful in describing experimental data for alkali Rydberg atoms prepared in a p state with principal quantum numbers $n>350$ [17]. Distinct quantum effects have so far been elusive. Quantum localization, i.e., the suppression of classical diffusion and ionization, would be one clear signature of classical-quantum discordance. Another one would be revivals [36]. Both of these features require the maintenance of phase coherence over many orbital periods T_{orb} and, therefore, tight control of stray fields in the experimental setup. We will in the following delineate the experimental parameter regime for which quantum localization should be observable. On a more fundamental level, the dependence of quantum localization on the number of degrees of freedom is of intrinsic interest. For the kicked atom with impulsive momentum transfers $\Delta\vec{p}$ along a fixed $(\hat{z})$ axis the L_z projection of the angular momentum is conserved. The system is therefore a time-dependent two degree of freedom system. Quantum localization is usually detected

as a suppression of ionization, i.e., the suppression of diffusive motion along the energy axis. The phase flow of the wave packet along a second degree of freedom, such as, e.g., the angular spread, is thus an open question. By contrast, when localization is detected in the recurrence probabilities, simultaneous freezing out of the diffusion in all degrees of freedom is implied. In fact, a recent study of the recurrence probability for the 3D atom [26] gave some indication of the occurrence of localization in low Rydberg states ($n \approx 10$). However, an extension to much higher n in order to make contact with the experiment as well as a comparative analysis of the classical phase-space structure in order to disentangle localization from stabilization on surviving tori, appears missing. We will in the following present an unequivocal characterization of the quantum localization in 3D in terms of three alternative measures: suppression of ionization, stability of the recurrence probability, and absence of quantum diffusion in a globally chaotic phase-space region. Moreover, we will identify Floquet states with a small imaginary part of the quasienergies scarred by unstable periodic orbits.

The plan of the paper is as follows: We start by presenting the method used for our numerical studies in Sec. II. The relation between the 3D kicked Rydberg atom and the previously studied 1D model is discussed in Sec. III. In Sec. IV we work through the different measures for quantum localization and identify a region in parameter space for an experimental verification of quantum localization. We present Floquet states and the ''scarring'' around unstable periodic orbits in Sec. V followed by a short summary. Atomic units are used unless otherwise stated.

II. METHOD

The experimental realization of the kicked Rydberg atom has been achieved by exposing alkali atoms with initial principal quantum number $n_i \approx 350$ to a train of up to about one hundred equispaced half-cycle pulses [25,30,37]. The pulses in the electric field $F(t)$ have a width T_p which is much shorter than the period of the unperturbed classical orbital motion, $T_p \ll T_{\mathrm{orb}} = 2\pi n_i^3$. Each ultrashort pulse therefore transfers a net momentum or ''kick'' to the electron [38],

$$\Delta \vec{p} = -\int \vec{F}(t)\,dt. \tag{2.1}$$

The kicked atom is described by the Hamiltonian

$$H(t) = H_{\mathrm{at}} + V(t), \tag{2.2}$$

where

$$H_{\mathrm{at}} = \frac{\vec{p}^2}{2} - \frac{1}{|\vec{r}|} \tag{2.3}$$

is the unperturbed atomic Hamiltonian. $\vec{p}$ and $\vec{r}$ are the momentum and position of the electron, respectively. The time-dependent perturbation is

$$V(t) = \vec{r} \cdot \vec{F}(t). \tag{2.4}$$

In this paper we focus on the unidirectionally kicked atom with constant kick strength, i.e., $\Delta \vec{p} = \Delta p z$ and $\Delta p > 0$. In this case, one can write $V(t) = zF(t)$ where

$$F(t) = -\Delta p \sum_{k=1}^{K} \delta(t + T/2 - kT). \tag{2.5}$$

Here T is the period of the kicks, and K the number of kicks. We place the kicks at the midpoint of the period T, i.e., the first kick comes at $t = T/2$. The frequency ν of the perturbation is defined as $\nu = 1/T$. The Hamiltonian (2.2) is cylindrically symmetric about the z axis and the magnetic quantum number is conserved. Throughout this paper we restrict ourselves to $m = 0$ and drop the index m.

We solve the time-dependent Schrödinger equation

$$i\frac{\partial}{\partial t}|\psi(t)\rangle = H(t)|\psi(t)\rangle \tag{2.6}$$

by means of the pseudospectral method [39]. Since the perturbation $V(t)$ [Eq. (2.4)] is periodic in time, the operator U describing the time evolution of the state after K periods,

$$|\psi(KT)\rangle = U(KT)|\psi(0)\rangle, \tag{2.7}$$

is completely determined by the period-one time-evolution operator $U(T)$, i.e.,

$$U(KT) = U(T)^K, \tag{2.8}$$

where

$$U(T) = \exp(-iH_{\mathrm{at}}T/2)\exp(i\Delta p z)\exp(-iH_{\mathrm{at}}T/2). \tag{2.9}$$

We note that Eq. (2.9) resembles the split operator algorithm which is, however, exact in the present case of delta-shaped kicks rather than an approximation to order T^3.

The free evolution operator

$$\exp(-iH_{\mathrm{at}}T/2) \tag{2.10}$$

is calculated in the energy representation, the eigenbasis of H_{at}, as

$$\exp(-iH_{\mathrm{at}}T/2)|nl\rangle = \exp(-i\varepsilon_{nl}T/2)|nl\rangle \tag{2.11}$$

with

$$\langle r\theta|nl\rangle = u_{nl}(r)Y_l(\cos\theta)/r. \tag{2.12}$$

Here $Y_l = Y_l^{m=0}$ are the spherical harmonics and ε_{nl} and $u_{nl}(r)$ are the eigenvalues and eigenfunctions of the radial Schrödinger equation,

$$\left(-\frac{d^2}{2dr^2} - \frac{1}{r} + \frac{l(l+1)}{2r^2}\right)u_{nl}(r) = \varepsilon_{nl}u_{nl}(r). \tag{2.13}$$

Solving Eq. (2.13) in a finite domain in coordinate space, $u_{nl}(r)$ coincides with the hydrogenic bound states with principal quantum number n for the lower portion of the spectrum $n<n_b$ (for a number n_b to be estimated below), whereas the eigenstates for u_{nl} with $n>n_b$ provide a discrete representation of the continuum. In general, n is referred to as the pseudostate number.

Evaluation of the boost operator

$$B=\exp(iz\Delta p) \tag{2.14}$$

in an atomic energy eigenbasis for high Rydberg states and continuum states has proven to be numerically difficult and unstable [40]. The operator is, however, diagonal in the coordinate representation. We therefore transform the time-evolved state $|\Psi(t)\rangle$ to a coordinate space representation $|\vec{r}\rangle=|r\,\theta\rangle$,

$$\langle r\,\theta|\psi(t)\rangle=\sum_l g_l(t,r)Y_l(\cos\theta), \tag{2.15}$$

where

$$g_l(t,r)=\sum_n \langle r\,\theta|nl\rangle\langle nl|\Psi(t)\rangle. \tag{2.16}$$

B mixes, however, the angular momenta l,

$$g_{l'}(t^+,r)=\sum_l g_l(t^-,r)[l'|\exp(ir\Delta p\cos\theta)|l], \tag{2.17}$$

where t^- and t^+ denote the time right before and right after a kick, respectively, and

$$[l'|\exp(ir\Delta p\cos\theta)|l] = \int_0^1 d(\cos\theta)Y_{l'}(\cos\theta)e^{ir\Delta p\cos\theta}Y_l(\cos\theta) \tag{2.18}$$

denotes a matrix element in angular momentum space while being still a local function in r. We evaluate the integral [Eq. (2.18)] by a Gauss-Legendre quadrature. Subsequently, we perform an inverse transformation back to the energy representation in order to evaluate the free evolution for the second half of the period [see Eq. (2.9)].

This scheme for solving the Schrödinger equation faces two numerical difficulties: the first one is to solve Eq. (2.13) for a large number of states subtending the continuum. The second difficulty is to calculate the transformation between the energy basis and the local radial coordinate basis efficiently for a large number of kicks without accumulating numerical errors. Both problems can be solved by means of the pseudospectral method.

Within the pseudospectral method a maximum radius $R^{\max}$ is chosen and the interval $r\in[0,R^{\max}]$ is mapped onto a new variable $x\in[-1,1]$ by a nonlinear mapping optimized for the Coulomb singularity. Within this interval we employ N collocation points. The mapped Hamiltonian is calculated numerically using the Legendre pseudospectral method. An example of the energy spectra ε_{nl} of the unperturbed Hamiltonian is shown in Fig. 1 for $l=0$. The lowest ε_{nl} values for $n<n_b$ are independent of l and agree with hydrogenic energies in up to 15 digits. The corresponding eigenfunctions agree with hydrogenic wave functions in up to 8 digits. This is true as long as $\langle r\rangle_n<R^{\max}$ where $\langle r\rangle_n=2n^2$ is the radius of the corresponding hydrogenic state. We thus have a cutoff for exact hydrogenic states, $n_b\lesssim\sqrt{R^{\max}/2}$. Thereafter, the pseudospectral energies ε_{nl} bend upwards, corresponding to the hard wall boundary conditions at $R^{\max}$. The eigenfunctions for $n>n_b$ represent states within the finite box with a wavelength of approximately $2R^{\max}/n$ and $\varepsilon_{nl}\approx(\pi n/R^{\max})^2/2$. This is true for n up to $n\approx N/2$ leading to a cutoff in energy, E_c, of the order of $(\pi N/R^{\max})^2/8$. The pseudostates with $n>n_b$ provide a discretized representation of the continuum. Since their density (for a given l) is $\rho(E)=\pi\sqrt{E/2}/R^{\max}$, the density of discretized states in the continuum can be controlled. The pseudospectral method is able to give a reliable representation of the states of the discretized continuum using as little as two grid points per half wave. Another advantage is that the transformation between energy basis and radial coordinate basis employs a Legendre quadrature, which can be performed to machine precision. This allows us to follow the long-time evolution with very good accuracy (10 000 kicks with a relative error less than 0.1%). The typical parameters for the calculations presented in this publication are $R^{\max}=2.5\times10^5$ a.u. and $N=1800$ leading to $E_c=6\times10^{-5}$ a.u. We include a maximum number of angular momenta in the calculations typically of the order of $l^{\max}=100$.

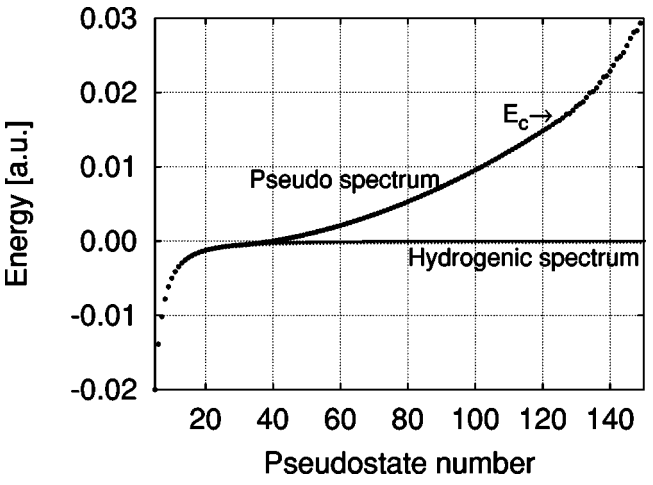

FIG. 1. Pseudospectrum for $R^{\max}=2000$ a.u., $N=250$, and $l=0$, which yields a cutoff energy $E_c\approx0.019$ (see text).

The numerical time propagation of wave functions that contain a significant admixture of continuum states always faces the difficulty of spurious reflections (see Ref. [41] and references therein). The present method allows to simultaneously control two types of reflections. The hard wall boundary conditions introduced at $r=R^{\max}$ can cause spurious reflections in coordinate space. We therefore employ ab-

sorbing boundary conditions by multiplying the wave function in the local coordinate representation $g_l(t,r)$ with the masking function

$$M_r(r)=\frac{1}{1+\exp[(r-R_c)/R_M]} \tag{2.19}$$

after each kick [42]. R_c and R_M are typically $0.8\,R^{\max}$ and $0.01\,R^{\max}$, respectively. In addition, there is a second class of reflections to be considered. As the kicks accelerate the electron to high positive energies, E can approach the cutoff energy E_c. After transformation to the energy basis, we therefore use an additional masking function for the pseudospectral basis $|nl\rangle$,

$$M_E(E)=\frac{1}{1+\exp[(E-E')/E_M]} \tag{2.20}$$

by which the wave function in the energy representation is multiplied after each time-evolution step. Typically, $E' \approx 0.8\,E_c$ and $E_M \approx 0.02\,E_c$. In our case of unidirectional kicks, the results are virtually independent of the shape of the masking functions, since any small portion of the wave function being spuriously reflected will be accelerated back towards the boundary by the following kicks. As a result of the masking in both coordinate and energy spaces, the time evolution ceases to be unitary. It is nevertheless possible to achieve a proper representation of the part of the Hilbert space relevant for the localization, since the masking eliminates only the outgoing continuum wave packet without affecting the bound-state or localized portion of the wave packet [29]. Note that apart form the discretization errors for finite N and cutoffs in $R^{\max}$ and $l^{\max}$, the method does not contain any further approximations. In particular, large values of the kick amplitude can be handled. This differs from the Cayley form of the boost operator, $\exp(iz\Delta p)\approx(1+iz\Delta p/2)/(1-iz\Delta p/2)$ used in Ref. [26], which is limited to small values of Δp.

In the following sections we will frequently use scaled units (i.e., all variables are measured in units of the initial Rydberg state), which we denote by the subscript ''0.'' These units are defined as $t_0=t/(2\pi n_i^3)$, $\nu_0=2\pi n_i^3/T$, $r_0=r/n_i^2$, $p_0=p\,n_i$, and $E_0=E\,n_i^2$.

III. RELATION BETWEEN THE 1D AND 3D MODELS

In our earlier studies of quantum localization we employed a 1D model [29,35] with the Hamiltonian

$$H^{1D}=\frac{p^2}{2}-\frac{1}{q}-qF(t), \tag{3.1}$$

where $q>0$ and p denote the position and momentum of the electron, respectively. The relation between the 3D dynamics and the 1D model has been also studied for the Rydberg atom driven by a microwave field [3,10,15,43,44]. It was observed that the agreement between the 1D and the 3D dynamics improves if a static electrical field is added in the direction of the initial state [44], a situation somewhat closer to unidirectional kicks. Unlike the harmonic driving field, the unidirectional field $F(t)$ defined by Eq. (2.5) allows for a distinction between the fields parallel ($\Delta p>0$) and antiparallel ($\Delta p<0$) to the elongated initial state. For the unidirectionally kicked atom, a close correspondence between the 1D and real 3D dynamics is only expected for $\Delta p>0$ [45].

To clarify the relation between the dynamics generated by the 3D Hamiltonian [Eq. (2.2)] and the 1D model [Eq. (3.1)], we express the 3D Hamiltonian in parabolic coordinates defined by $\xi=r+z$, $\eta=r-z$, and $\tan\phi=y/x$,

$$H(\xi,\eta,\phi)=-\frac{1}{2}\left\{\frac{4}{\xi+\eta}\frac{d}{d\xi}\left(\xi\frac{d}{d\xi}\right)+\frac{4}{\xi+\eta}\frac{d}{d\eta}\left(\eta\frac{d}{d\eta}\right)+\frac{1}{\xi\eta}\frac{d^2}{d\phi^2}\right\}-\frac{2Z}{\xi+\eta}+\frac{\xi-\eta}{2}F(t). \tag{3.2}$$

Here, $Z=1$ is the nuclear charge. In the following we consider only $m=0$ and drop all m and ϕ dependent terms.

The static part of Eq. (3.2) is separable in parabolic coordinates and yields the well-known parabolic states $\phi^P(\vec{r})=u_1(\xi)\,u_2(\eta)$ [46], examples of which for high Rydberg states ($n=100$) are displayed in Fig. 2 and which will be employed in the following as initial states at $t=0$. Parabolic states can be labeled by the principal quantum number n, and the parabolic quantum numbers n_1,n_2 with the constraint $n=n_1+n_2+|m|+1$. We consider in the following n and n_2 to be the independent variables by which we label the states. The factor functions $u_{1,2}$ are solutions to the equation

$$\left[-\frac{d}{dg}\left(g\frac{d}{dg}\right)-\frac{Eg}{2}-Z_{1,2}\right]u_{1,2}(g)=0. \tag{3.3}$$

Here, g stands for ξ and η, respectively, $E=-1/(2n^2)$, and the separation constants are $Z_1=(n-n_2-1/2)/n$ and $Z_2=(n_2+1/2)/n$. We focus in the following on elongated initial states with $n_2^i \ll n_i$, for which a close connection to the 1D problem is expected to emerge.

Let us assume for a moment that the separation ansatz $\Psi(\xi,\eta,t)=u_1(\xi,t)u_2(\eta,t)$ valid at $t=0$ for parabolic initial states remains valid also for $t>0$. Using this ansatz, the time-dependent Schrödinger equation multiplied by $(\xi+\eta)/(2u_1u_2)$ becomes

$$i\frac{\xi+\eta}{2}\left[\frac{\dot{u}_1}{u_1}+\frac{\dot{u}_2}{u_2}\right]=-\frac{1}{u_1}\frac{d}{d\xi}\left(\xi\frac{d}{d\xi}\right)-\frac{1}{u_2}\frac{d}{d\eta}\left(\eta\frac{d}{d\eta}\right)-Z_1(t)-Z_2(t)+\frac{(\xi^2-\eta^2)}{4}F(t). \tag{3.4}$$

Here, $Z_1(t)$ and $Z_2(t)$ are the time-dependent separation constants subject to the condition $Z_1(t)+Z_2(t)=Z$.

The initial expectation values of ξ and η at $t=0$ are

$$\langle u_1|\xi|u_1\rangle=n_i(n_1^i+1/2)=n_i(n_i-n_2^i-1/2), \tag{3.5a}$$

$$\langle u_2|\eta|u_2\rangle=n_i(n_2^i+1/2). \tag{3.5b}$$

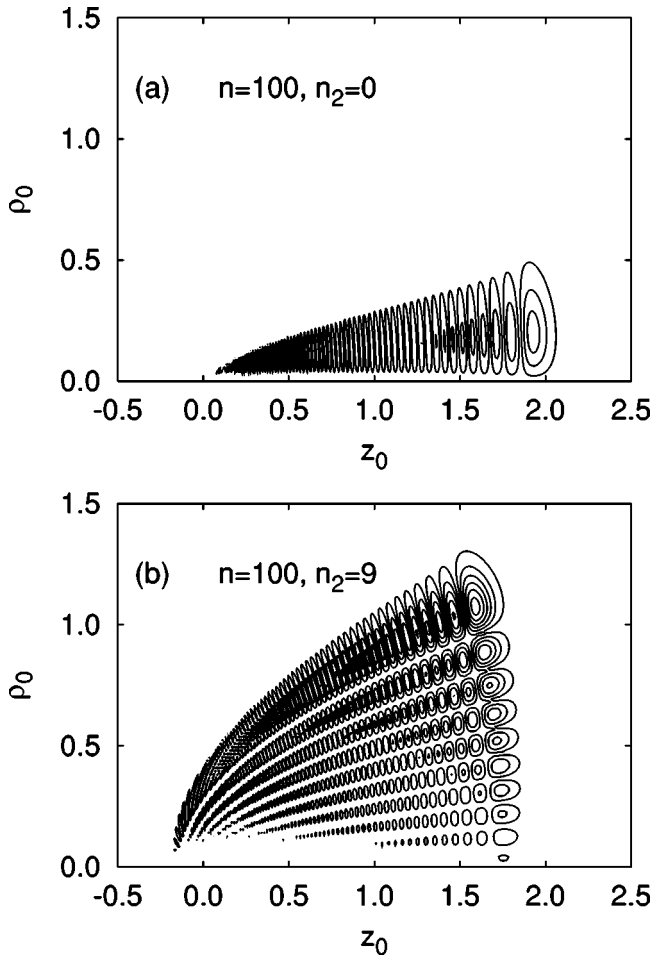

FIG. 2. Contour plots of the probability density of parabolic states in the $n=100$ shell of hydrogen for (a) $n_2=0$ corresponding to the extreme parabolic state with maximal elongation, and (b) $n_2=9$ corresponding to a strongly polarized state. The figure is drawn in scaled cylindrical coordinates z_0 and $\rho_0=\sqrt{x_0^2+y_0^2}$.

We consider first the equation of motion for $u_1(\xi,t)$ which, in the limit of $n_2^i/n_i \to 0$, accounts for the motion in the direction of the kicks. In this limit, $\langle \eta \rangle \ll \langle \xi \rangle$ and we can neglect terms proportional to η on the left-hand side of Eq. (3.4). Collecting terms in Eq. (3.4) containing ξ and u_1 and using $Z_1(t) \approx Z_1(0) \approx 1$ and $Z_2(t) \ll Z_1$ we arrive at

$$i\dot{u}_1(\xi,t)=\left[-2\frac{d^2}{d\xi^2}-\frac{2}{\xi}\frac{d}{d\xi}-\frac{2}{\xi}+\frac{\xi}{2}F(t)\right]u_1(\xi,t). \tag{3.6}$$

Noting that in the limit of an elongated state $\xi=r+z\approx 2z$ for $z>0$, Eq. (3.6) reduces to

$$i\dot{u}_1(z,t)=\left[-\frac{1}{2}\frac{d^2}{dz^2}-\frac{1}{2z}\frac{d}{dz}-\frac{1}{z}+zF(t)\right]u_1(z,t). \tag{3.7}$$

After transforming the wave function according to $u_1(z,t)=\psi_1(z,t)/\sqrt{z}$ we find the effective Schrödinger equation

$$i\dot{\psi}_1(z,t)=\left[-\frac{1}{2}\frac{d^2}{dz^2}+\frac{\tilde{\lambda}^2}{2z^2}-\frac{1}{z}+zF(t)\right]\psi_1, \tag{3.8}$$

with the pseudoangular momentum $\tilde{\lambda}^2=-1/2$. For $n_i \geqslant 100$ the spatial extension of the wave function is of the order of 10^4 a.u. and the Coulomb term is 10^4 times larger than the ''centrifugal'' term. Consequently, neglecting the ''centrifugal'' term $\tilde{\lambda}^2/2z^2$, the 1D kicked Rydberg atom [Eq. (3.1)] is recovered.

We turn now to the motion in the η degree of freedom. In order for the separation ansatz to remain approximately valid, the excursion in η should remain small compared to that of ξ. We explore the condition under which the separability remains valid. To this end, we collect all terms in Eq. (3.4) containing u_2 and η to arrive at

$$i\frac{1+\xi/\eta}{2}\dot{u}_2=\left[-2\frac{d^2}{d\eta^2}-\frac{2}{\eta}\frac{d}{d\eta}-\frac{2Z_2(t)}{\eta}-\frac{\eta}{2}F(t)\right]u_2. \tag{3.9}$$

Replacing ξ/η by their initial expectation values $\langle \xi \rangle / \langle \eta \rangle = \beta^{-1}=(n_i-n_2^i-1/2)/(n_2^i+1/2) \gg 1$, substituting $\eta=2s$, and proceeding in analogy to Eq. (3.8), we find

$$i\frac{d\psi_2(t)}{d(\beta t)}=\left[-\frac{1}{2}\frac{d^2}{ds^2}+\frac{\tilde{\lambda}^2}{2s^2}-\frac{Z_2(t)}{s}-sF(t)\right]\psi_2(t). \tag{3.10}$$

In order to transform Eq. (3.10) again into the standard form of the 1D kicked hydrogen atom we assume $Z_2(t) \approx Z_2(0)$ and rescale variables as

$$\tilde{s}=sZ_2,$$

$$\tilde{p}=p/Z_2,$$

$$\tilde{t}=\beta Z_2^2 t, \tag{3.11}$$

leading to

$$i\frac{d}{d\tilde{t}}\psi_2(\tilde{t},\tilde{s})=\left[-\frac{1}{2}\frac{d^2}{d\tilde{s}^2}+\frac{\tilde{\lambda}}{2\tilde{s}^2}-\frac{1}{\tilde{s}}-\tilde{s}\tilde{F}(\tilde{t})\right]\psi_2(\tilde{t},\tilde{s}) \tag{3.12}$$

with

$$\tilde{F}(\tilde{t})=\beta\Delta\tilde{p}\sum_k \delta(\tilde{t}-k\tilde{T}+\tilde{T}/2). \tag{3.13}$$

The strength of the field [Eq. (3.13)] is very small due to the factor $\beta \ll 1$ and further, the direction of the kicks is inverted compared to Eq. (3.8) and points *towards* $\tilde{s}=0$. For kicks towards the nucleus, classical stabilization takes place. The classical phase space is mixed and the classical as well as the quantum system can be either stable and nondiffusive or chaotic [25,30]. We therefore expect the dynamics corresponding to the Hamiltonian Eq. (3.12) to be either stable or dif-

fusive at a small rate. Depending on the parameters chosen, the motion in the η degree of freedom may therefore remain confined and the approximate separability of the 3D system may be preserved for some time. In this case, chaotic diffusion proceeds mainly in the ξ coordinate of the 3D system closely resembling the corresponding 1D system. In general, however, the motion in the η degree of freedom is chaotic and the separation ansatz will break down for long times. There are two scenarios for this: Either the initial state $\psi_2(\tilde{t}=0)$ resides in the chaotic sea from the onset, or the motion in the ξ coordinate induces a parametric time dependence of Z_2 and β allowing trajectories initially residing in islands that are stable as long as the dynamics in ξ and η are decoupled to diffuse into the chaotic sea of the coupled dynamics in analogy to Arnold diffusion and escape to infinity. Quantum localization, if operational, must therefore suppress classical diffusion in both degrees of freedom. Note that in the opposite case $\Delta p<0$, the kicks in Eq. (3.12) are directed away from the nucleus and a much less good agreement between the 1D model and the real 3D dynamics can be expected [45]. We will numerically investigate the scenario $\Delta p>0$ for the full 3D classical and quantum dynamics below.

IV. NUMERICAL EVIDENCE FOR QUANTUM LOCALIZATION

In this section we probe different measures of quantum localization for the 3D kicked Rydberg atom. In order to identify quantum localization instead of trapping in stable islands, the initial state should be located in the chaotic region of phase space. We therefore start by analyzing the classical dynamics.

A. Classical dynamics and the initial state

In Fig. 3 we show classical stroboscopic Poincaré surface of sections for $\nu_0=4$ and $\Delta p_0=0.0314$. ($\rho_0=\sqrt{x_0+y_0}$ is a cylindrical coordinate.) Negative z_0 values correspond to the side of the nucleus where the kicks are directed towards the nucleus. On this side we find many stable islands [Fig. 3(a)] similar to the stable islands found in the 1D model for negative kicks (leading to classical stabilization). In 3D these islands have a finite width in ρ_0 and p_{ρ_0} [Fig. 3(b)]. For positive z_0, on the other hand, we find no stable islands at all [Figs. 3(a) and 3(c)]. To study quantum localization we therefore will choose initial conditions corresponding to states located at $z_0>0$.

The parabolic eigenstates, as discussed in Sec. III and shown in Fig. 2, are good candidates for locating the initial state outside any stable islands. We note that the expectation value of the polar angle of the position vector $\vec{r}$, $\cos\hat{\theta}=\hat{z}/\hat{r}$, for a parabolic state is given via the hypervirial theorem [47] by

$$\langle \phi^P_{n,n_2}|\cos\hat{\theta}|\phi^P_{n,n_2}\rangle=-\langle \phi^P_{n,n_2}|\cos\hat{\theta}_{\mathrm{RL}}|\phi^P_{n,n_2}\rangle. \quad (4.1)$$

Here, $\hat{\theta}_{\mathrm{RL}}=\cos^{-1}(A_z/|\vec{A}|)$ is the polar angle of the Runge-Lenz vector $\vec{A}$,

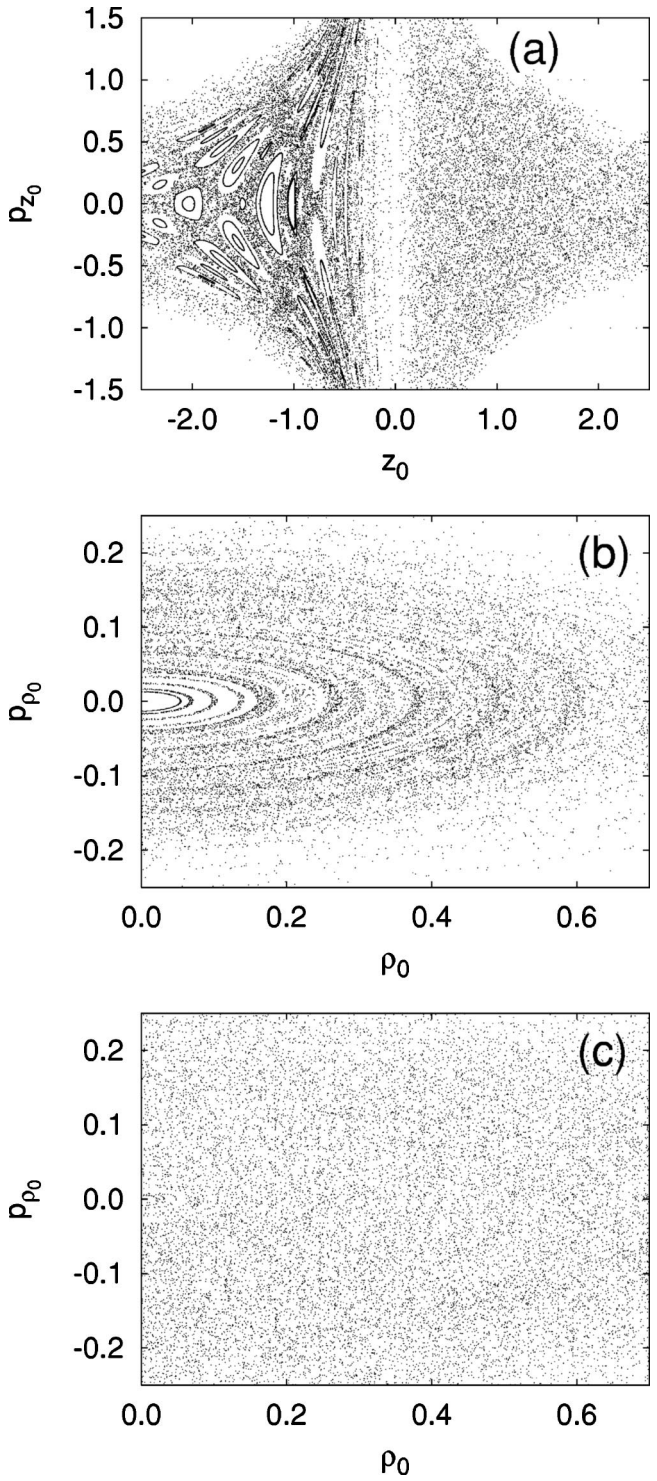

FIG. 3. Classical stroboscopic Poincaré surfaces of section for the 3D kicked atom with $\Delta p_0=0.0314$ and $\nu_0=4$. Cuts at (a) $\rho_0=0.1$ and $p_{\rho_0}=0$, (b) $z_0=-2.0$ and $p_{z_0}=-0.05$, and (c) $z_0=+2.0$ and $p_{z_0}=-0.05$. The cuts in time are taken half a period after each kick.

$$\vec{A}=\vec{p}\times\vec{L}-\vec{r}/|\vec{r}|, \quad (4.2)$$

which points to the perihelion of a Kepler orbit. Note that the operator equivalence (4.1) holds for all states of a given n shell. Likewise, it holds for classical ensemble averages for a

given energy shell. The right-hand side of Eq. (4.1) can be further expressed as

$$\langle \phi^P_{n,n_2} | \cos\theta_{\rm RL} | \phi^P_{n,n_2} \rangle = (2n_2+1)/n - 1. \qquad (4.3)$$

Consequently, we can select subensembles of classical initial conditions representing orbits of a given parabolic state by selecting A_z from within the bin

$$(n_2^i - 0.5)/n_i < (1+A_z)/2 < (n_2^i + 0.5)/n_i . \qquad (4.4)$$

The extreme parabolic state with $n_2^i = 0$ is strongly localized near the z axis with $\langle \cos\theta \rangle = 1 - 1/n_i$. States with larger n_2^i, on the other hand, correspond to "true" 3D states showing a larger spread in ρ_0. In view of the Poincaré surface of section (Fig. 3) we will choose a parabolic initial state elongated in the direction of the kicks with $n_2^i \ll n_i$ in order to ensure that the initial state lies completely inside the chaotic sea. In the following we focus on $n_i = 100$ and $n_2^i = 0$ or $n_2^i = 9$. The second choice is motivated by recent experimental realization of highly elongated "parabolic" states in very high n (≈ 350) by photoexciting Rydberg atoms in the presence of a small dc field. Values of $\langle \cos\theta \rangle \gtrsim 0.8$ have been reached [48].

B. Survival probability

We explore now the parameter ranges of Δp_0 and ν_0 for the observation of quantum localization. Based on previous studies on the 1D kicked atom [29,35] as well as on the harmonically driven 1D and 3D Rydberg atom [3,10,15], localization is expected in the high-frequency domain, $\nu_0 > 2$. The range of experimentally available high frequencies is limited by the condition that adjacent pulses must be well separated from each other, i.e., the width T_p of the pulses must be smaller than the period $T = T_{\rm orb}/\nu_0$ of the kicks. Consequently we require $\nu_0 \ll T_{\rm orb}/T_p$. The experimentally realized T_p is of the order of 0.5 ns and $T_{\rm orb} = 2\pi n_i^3$ is for $n_i = 350$ of the order of 6 ns, which implies that ν_0 should be limited to $\nu_0 \lesssim 4$ if we require that the spacing between the pulses is at least the threefold width ($T_{\rm orb}/\nu_0 > 3T_p$), in order to approximately fulfill the requirement of successive impulsive perturbations.

For the choice of kick strengths, we note that unidirectional kicks build up an average field with $F^{\rm av} = -\Delta p/T$. Hence the Hamiltonian [Eq. (2.2)] can be cast into the time-independent Stark Hamiltonian

$$H_{\rm Stark} = H_{\rm at} + zF^{\rm av} \qquad (4.5)$$

plus an infinite series of higher harmonics of equal strength,

$$H(t) = H_{\rm Stark} + 2F^{av} z \sum_{m=1}^{\infty} \cos\left[2\pi m/T \left(t - \frac{T}{2} \right) \right]. \qquad (4.6)$$

The Hamiltonian [Eq. (4.6)] can be reduced to the one for the harmonically driven Rydberg atom with field strength $2F^{\rm av}$ by keeping only the $m = 1$ term. Equation (4.6) suggests both similarities and differences between the kicked Rydberg atom and the harmonically driven system. For example, the

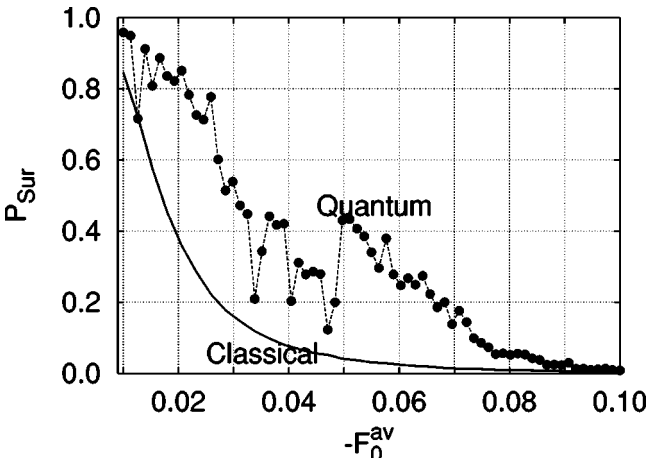

FIG. 4. Quantum and classical survival probabilities after $K = 500$ kicks as a function of average field $F_0^{av} = -\Delta p_0 \nu_0/2\pi$ for $\nu_0 = 4$, $n_i = 100$, and $n_2^i = 0$.

critical field strength for the harmonically driven classical system to be globally diffusive is $|2F_0^{\rm crit}| \approx 1/(50\nu_0^{1/3})$ [3]. For the frequency range of the present study this would correspond to $F_0^{\rm crit} \approx 0.013$. By contrast, the 1D positively kicked Rydberg atom is chaotic for an arbitrarily small field strength. Similarly, as the localization theory for the harmonically driven quantum system explicitly invokes the presence of only a single harmonic component in the driving field corresponding to a nearest-neighbor coupling in the Anderson model, quantum localization in the kicked atom with all harmonics present at equal strength (corresponding to an all-site coupling of the lattice) will be in general more complex.

We now study the classical and quantum survival probabilities for the kicked Rydberg atom as a function of the scaled average field $F_0^{av} = F^{av} n_i^4$. The quantum survival probability (Fig. 4) is determined from

$$P_{\rm sur}(t) = \sum_{n({\rm bound})} \sum_{l} |\langle nl | \psi(t) \rangle|^2, \qquad (4.7)$$

while classical survival probabilities are deduced from the fraction of electrons being bound at time t. The average field in the Stark Hamiltonian [Eq. (4.5)] leads to a decay via classical field ionization even without the time-dependent perturbation present when $|F^{\rm av}|$ is larger than the Stark threshold at $|F_0^{\rm av}| = 1/16 = 0.0625$. The classical survival probability for the kicked atom decays within the first few hundred kicks close to and above the threshold. Rapid classical ionization is convenient for the observation of quantum localization, implying that we should choose $|F_0^{\rm av}| > 0.01$. A first indication of quantum localization is that the quantum survival probability exceeds the classical one, since this implies a suppression of diffusion towards the threshold. The quantum survival probability after $K = 500$ is, unlike the classical survival probability, fluctuating as a function of F_0^{av} (Fig. 4). However, in the region $0.01 < |F_0^{av}| < 1/16$, it is consistently much larger than the classical value. For our studies, we will choose field strengths $F_0^{\rm av} \approx -0.02$. Note that for

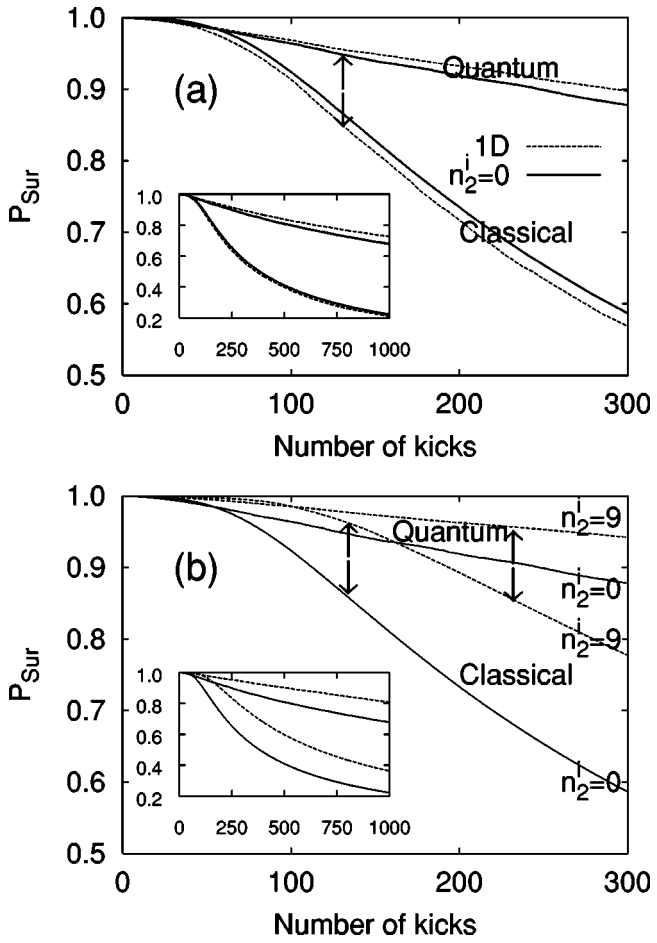

FIG. 5. Survival probabilities $P_{\rm sur}$ for $F_0^{\rm av}=-0.02$, $\nu_0=4$, and $n_i=100$ for the classical and quantum kicked Rydberg atoms. In (a) we show 3D results for $n_2^i=0$ (full lines) and 1D model results (dashed lines). In (b) the 3D results for $n_2^i=0$ (full lines) and for $n_2^i=9$ (dashed lines) are shown. The arrows mark the number of kicks K_L where the quantum survival probability is larger than the classical one by 0.1 and localization sets in. Insets: long-time behavior.

our parameters ($\nu_0=4$ and $n_i=100$), the energy difference between the initial state and the energy of the Stark barrier at $-2\sqrt{-F_0^{\rm av}}$ is equal to the energy of about six photons ($E_0^\gamma=\nu_0/n_i$) for the fundamental harmonic. The time evolution of the quantum and classical survival probabilities, as shown in Fig. 5, also displays quantum values well above the classical ones. In addition, the 1D results and the 3D results for the most elongated parabolic state ($n_2^i=0$) closely resemble each other, as expected from our analysis in Sec. III.

It is of particular interest that the suppression of ionization prevails when we increase n_2^i to cases where already the initial state explores the transverse degree of freedom. Also for $n_2^i=9$ [Fig. 5(b)], a clear signature of quantum localization can be seen. Further, both the classical and the quantum survival probabilities are larger for $n_2^i=9$ as compared to $n_2^i=0$. The latter observation can be understood from the fact that ionization proceeds mainly along the ''reaction coordinate'' z. States that have a larger spread perpendicular to z (i.e., larger n_2^i) are therefore more stable against ionization

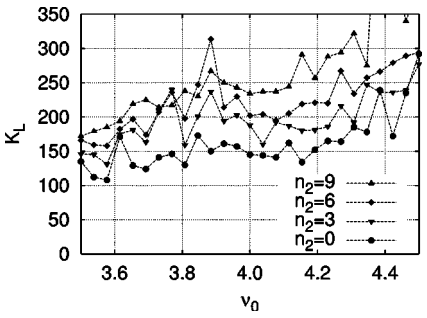

FIG. 6. Localization number of kicks K_L at which the quantum survival probability becomes larger than the classical one by 0.1 as a function of frequency ν_0 for $F_0^{\rm av}=-0.02$, $n_i=100$, and different n_2^i.

as they are less likely to visit the saddle point region [43]. To verify that the suppression of ionization as seen for our particular choice of parameters is not accidental, we study the survival probability as a function of both ν_0 and n_2^i. We define an empirical measure in terms of the number of kicks K_L where the quantum survival probability exceeds the classical one by 10%, $P_{\rm Sur}^{\rm Quant}(K_L)-P_{\rm Sur}^{\rm Classic}(K_L)=\Delta P_{\rm Sur}=0.1$ (in Fig. 5 K_L is indicated by arrows). This measure may be useful to guide the experiment for identifying localization. Figure 6 reveals that K_L, on average, increases with ν_0. This is due to the fact that for a fixed average field F_0^{av}, $\Delta p_0=-2\pi F_0^{av}/\nu_0$ decreases as ν_0 increases. This implies longer lifetimes in the units of K. We further see that K_L increases with n_2^i. This increase is a direct reflection of the fact that the system becomes more stable as n_2^i increases, as discussed above.

We note that the decay rate of the quantum system is still fairly large. This is a consequence of the presence of high harmonics in the driving field [Eq. (4.6)]. The latter allows a direct one-photon (a well as multiphoton) ionization. We estimate the direct coupling to the continuum by single-photon ionization by applying first-order perturbation theory (the golden rule) to calculate the decay rates. The Stark Hamiltonian [Eq. (4.5)] in the 1D model is diagonalized on a finite grid using the pseudospectral method and we sum the decay rates over all harmonic components in the driving field with an energy large enough to couple the Stark state with the largest overlap to the initial Rydberg state to the Stark continuum. The sum of the decay rates leads to a lifetime in scaled units of $\tau_0=760$. At $K=1000$ this corresponds to a survival probability of $P_{\rm Sur}=0.720$, which is practically identical to the value $P_{\rm Sur}(K=1000)=0.725$ numerically found for the *kicked* Rydberg atom. We thus conclude that ionization due to diffusive spreading of the wave packet (as opposed to direct photoabsorption) is practically absent in the kicked system.

In view of the presence of the direct ionization channel, it is instructive to consider an alternative measure for localization which is more directly focused on the initial state, namely, the recurrence probability,

$$P_{\rm rec}(K)=|\langle\psi(0)|\psi(KT)\rangle|^2. \tag{4.8}$$

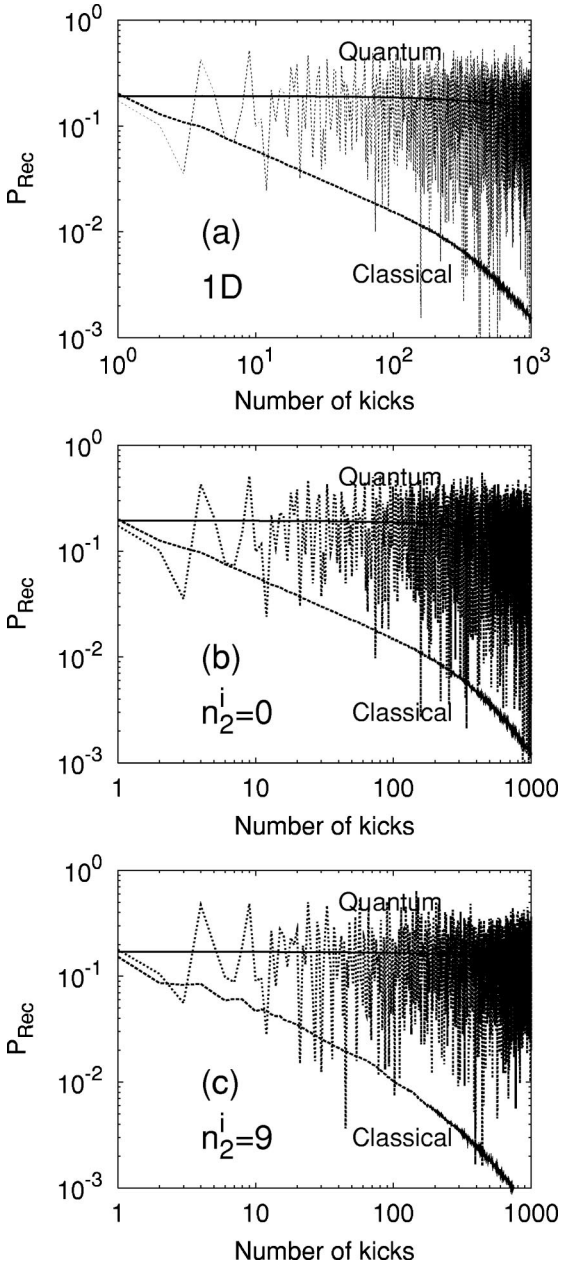

FIG. 7. Quantum and classical recurrence probabilities for (a) the 1D model and the full 3D system with (b) $n_2^i=0$ and (c) $n_2^i=9$. The full line indicates a fit of the quantum data to a third-order polynomial ($\nu_0=4$, $F_0^{\rm av}=-0.02$, and $n_i=100$).

The classical recurrence probability is the probability for the electron to be in an energy and angle bin corresponding to the initial state. The quantum recurrence probabilities for both the 1D and the 3D cases (Fig. 7) are strongly fluctuating, which is a signature of quantum beats. Their average value is, however, much larger than the classical value, indicating the suppression of diffusion away from the initial state. Further note that the decay of the classical recurrence probability is stronger for $n_2^i=9$ than for $n_2^i=0$, indicating a stronger diffusion in the parabolic degree of freedom for the less elongated classical state.

Since current experiments are primarily performed at very high $n_i\approx 350$, we analyze the dependence of K_L on n_i in order to assess the chance for experimental observation of quantum localization (Fig. 8). Apart from some fluctuations, K_L remains more or less constant as a function of n_i within the range of n_i currently computationally accessible ($n_i\lesssim 150$). The remarkably weak dependence on n_i can be understood from the fact that the rapid classical decay is scale invariant while the residual quantum decay, as a result of quantum localization, is governed by direct photon coupling to the continuum. Calculating, as described above, the lifetime τ_0 assuming only the direct single-photon ionization from the initial state through the higher-order components of the driving field to be relevant, we find for $\nu_0=4$ that $\tau_0(n_i=50)=520$, $\tau_0(n_i=100)=760$, and $\tau_0(n_i=150)=825$. Assuming an exponential decay with these lifetimes for the quantum system and comparing to the classical survival probability, the localization times are $K_L=135$, 125, and 124 for $n_i=50$, 100, and 150, respectively. These variations are much smaller than the fluctuations with ν_0 seen in Fig. 8.

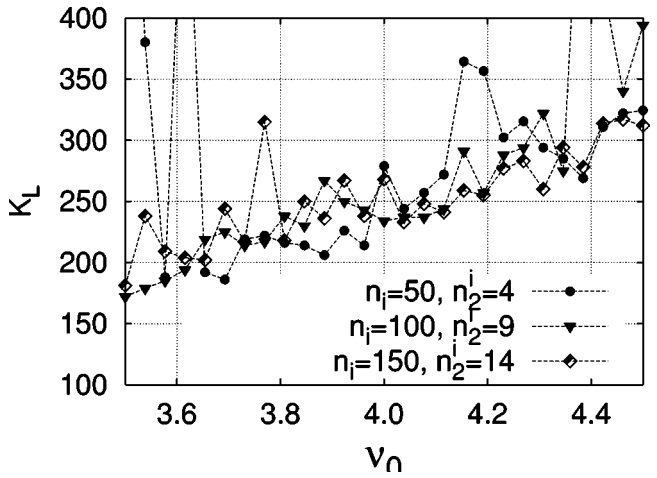

FIG. 8. Localization number of kicks K_L as a function of frequency ν_0 for $F_0^{\rm av}=-0.02$ and different n_i for initial states with a width in the angular degree of freedom $\langle\cos\theta\rangle=1-1/n_i-2n_2^i/n_i\approx 0.8$.

The most important point is that quantum localization exists over a wide range of ν_0, n_i, and n_2^i. Extrapolating the weak n_i dependence to higher n_i leads to the prediction that the suppression of classical ionization by quantum localization should be measurable for $\nu_0\approx 4$ and $F_0^{\rm av}\approx -0.02$ within 200–300 kicks even at $n_i\approx 350$ provided the initial state in the experiment is prepared in a strongly elongated state with $\langle\cos\theta\rangle\gtrsim 0.8$. This parameter range appears to be accessible in current experiments.

C. Spreading of the wave function

Quantum localization implies that the quantum wave packet remains well localized whereas the corresponding classical density distribution diffuses strongly. This is expected to hold for *all* degrees of freedom. We first consider the reduced density as a function of energy which measures the spread in energy and, in the present case, also the spread along the reaction coordinate z (or ξ),

$$\rho_0((E_n)_0,K)=\begin{cases}\displaystyle\sum_{n_2'} |\langle n\, n_2'|\psi(K)\rangle|^2/\Delta(E_n)_0 \quad \text{(quantum)} & \text{(4.9a)}\\ \displaystyle\int_{(\tilde{E}_n)_0<(E_n)_0<(\tilde{E}_{n+1})_0} d\vec{r}d\vec{p}f(\vec{r},\vec{p},K)/\Delta(E_n)_0 \quad \text{(classical)}, & \text{(4.9b)}\end{cases}$$

where $(\tilde{E}_n)_0=[(E_{n-1})_0+(E_n)_0]/2$, $\Delta(E_n)_0=[(E_{n+1})_0-(E_{n-1})_0]/2$, and $f(\vec{r},\vec{p},K)$ is the classical phase-space distribution after K kicks. Note that the initial density in both the quantum and the classical cases has a narrow peak at scaled energy $E_0=-0.5$. The densities shown in Fig. 9 peak at around $E_0=-0.5$ and clearly reveal that the quantum distribution in energy is much narrower than the classical one after a large number of kicks K for all cases. We find localization in the 3D case along the energy coordinate for $n_2^i=0$ as well as for $n_2^i=9$. Moreover, the energy distribution of the 1D kicked Rydberg atom mimics the distribution in 3D.

We consider now the reduced density as a function of the ''transverse'' degree of freedom, i.e., as a function of the scaled parabolic quantum number $(n_2)_0=n_2/n_i$,

$$\rho_0((n_2)_0)=\begin{cases} n_i\displaystyle\sum_{n'n_2'} |\langle n' n_2'|\psi(K)\rangle|^2 & \text{(quantum)}\\ n_i\displaystyle\int d\vec{r}d\vec{p}f(K,\vec{p},\vec{r}) & \text{(classical)}\end{cases} \tag{4.10}$$

subject to the constraint

$$(n_2)_0-0.5/n_i\leqslant n_2'/n'\leqslant(n_2)_0+0.5/n_i \quad \text{(quantum)},$$

$$(n_2')_0-0.5/n_i\leqslant(1+A_z)/2\leqslant(n_2)_0+0.5/n_i \quad \text{(classical)}. \tag{4.11}$$

To characterize the localized part of the wave function, the sum in Eq. (4.10) is taken over only bound states, and correspondingly the integral is limited to $E\leqslant 0$. The quantum distribution $\rho_0((n_2)_0)$ remains well localized for the maximally elongated initial state which corresponds to a narrow peak at $(n_2^i)_0=0$ [Fig. 10(a)] as well as for the state with moderate transverse excitation [$(n_2^i)_0=0.09$, Fig. 10(b)]. In both cases, the quantum distributions remain considerably more confined compared to their classical counterparts.

As a byproduct, we find that quantum localization in n_2 justifies the applicability of earlier 1D simulations since quantum mechanics remains practically one dimensional. On the contrary, the classical system spreads in the parabolic degree of freedom and explores the full three-dimensional space. This indicates a stronger coupling between the dynamics along ξ and η (in line with the discussion in Sec. III). Not only the diffusion along ξ but also the coupling to η is quantum mechanically suppressed. Thus quantum localization in *all* dimensions is observed.

V. FLOQUET STATES: WAVE FUNCTIONS AND HUSIMI DISTRIBUTIONS

We consider now the Floquet states rather than the time-evolved wave packet. They are the eigenstates of the period-one time-evolution operator [Eq. (2.9)]. The Floquet states $|\phi^F\rangle$ satisfy the eigenvalue equation

$$U(T)|\phi_j^F\rangle=\exp(-iT\mathcal{E}_j)|\phi_j^F\rangle \tag{5.1}$$

with the complex quasienergies $\mathcal{E}_j=\mathcal{E}_j^R-i\mathcal{E}_j^I$. The time-evolved wave packet $|\Psi(KT)\rangle$ can be written as a coherent superposition of Floquet states,

$$|\psi(KT)\rangle=\sum_j d_j\exp(-iKT\mathcal{E}_j)|\phi_j^F\rangle, \tag{5.2}$$

where $d_j=\langle\psi(0)|\phi_j^F\rangle$.

Due to the finite size used in our numerical calculations, i.e., the cutoffs in radius and energy, $U(T)$ is nonunitary and the imaginary part $\mathcal{E}_j^I$ describes a probability flux out of the finite Hilbert subspace considered. Provided that the subspace is large enough to represent resonances and localized states, the flux out of the finite Hilbert space corresponds to a physical flux away from the atom (rather than a numerical artifact) and small $\mathcal{E}_j^I$ can be interpreted as the inverse lifetime of Floquet states, i.e., $\Gamma_j/2=\mathcal{E}_j^I$ [49]. Moreover, Floquet-states with very small Γ_j can be candidates for states representing quantum localization. Note that due to the presence of the direct one-photon ionization channel, a localized state will have a nonvanishing value of Γ_j.

In the 1D case, we can obtain Floquet states by diagonalizing a matrix representation of $U(T)$ in the pseudospectral basis. Unfortunately, the matrix $U(T)$ in the 3D case is a very large matrix the size of which is $(l^{\max}*N/2)\times(l^{\max}*N/2)$. Typically, $(l^{\max}*N/2)\approx 10^5$ and the matrix is not sparse since the kick mixes all energies and angular momenta. Direct diagonalization is thus out of reach. Instead, we extract the relevant $\mathcal{E}_j$ from the autocorrelation function by means of harmonic inversion [50]. The autocorrelation function is defined as the projection of the evolved wave packet onto the initial state,

$$a(KT)=a_K=\langle\psi(0)|\psi(KT)\rangle=\langle\psi(0)|U(T)^K|\psi(0)\rangle$$

$$=\sum_j d_j^2\exp(-iK\varepsilon_jT). \tag{5.3}$$

In order to calculate the relevant Floquet states, $U(T)$ is expanded in a reduced set with basis functions $|\beta_n\rangle=U^n|\beta_0\rangle$ where $|\beta_0\rangle=|\psi(0)\rangle$ is the initial state. Because of

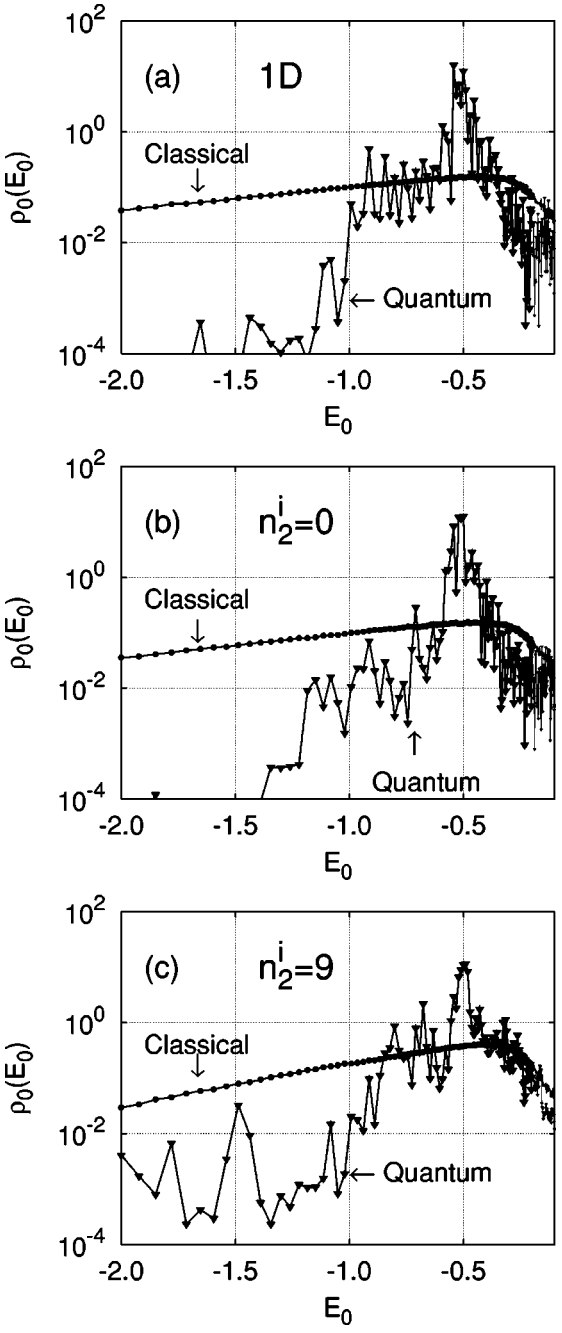

FIG. 9. Quantum and classical probability densities in energy for $n_i=100$ after $K=1000$ kicks with $\nu_0=4$ and $F_0^{\rm av}=-0.02$ for (a) the 1D model and the full 3D system with (b) $n_2^i=0$ and (c) $n_2^i=9$.

the symmetry $U^t(T)=U(T)$, where the superscript t stands for transposition, we denote $\langle\beta_n|$ as the transpose of $|\beta_n\rangle$ (but not the Hermite conjugate). Thus $\langle\beta_n|=\langle\beta_0|(U^n)^t=\langle\beta_0|U^n$, which leads to the matrix elements of $U(T)$,

$$U_{nn'}=\langle\beta_n|U(T)|\beta_{n'}\rangle=a_{n+n'+1}. \tag{5.4}$$

Since the set of states $|\beta_n\rangle$ $(n=1,2,3,\ldots)$ is not an orthogonal set, one must solve a generalized nonunitary eigenvalue problem to obtain the Floquet states,

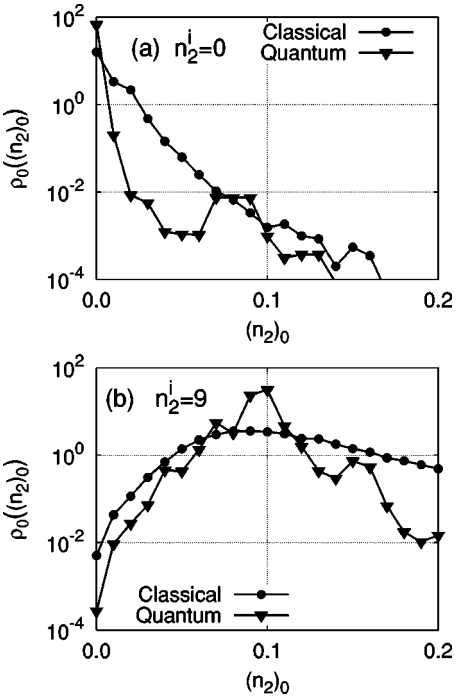

FIG. 10. Classical and quantum probability densities as a function of the parabolic quantum number $(n_2)_0$ after $K=1000$ kicks for (a) $n_2^i=0$ and (b) $n_2^i=9$ ($\nu_0=4$, $F_0^{\rm av}=-0.02$, and $n_i=100$).

$$\sum_{n'} U_{nn'}b_{n'}^{(j)}=\sum_{n'} e^{-iT\varepsilon_j}S_{nn'}b_{n'}^{(j)} \tag{5.5}$$

with the overlap matrix $S_{nn'}=a_{n+n'}$. The resulting eigenvalues and eigenfunctions in the restricted basis give the quasienergies and coefficients d_j only for those Floquet states that have sizable overlap with the initial state. Typically, less than 1000 Floquet states contribute to the autocorrelation function, restricting the size N_β of the basis set $|\beta_n\rangle$ to less than 1000. Indeed, using too large a value of N_β, the diagonalization becomes unstable since the null space of the matrix $U_{nn'}$ becomes large (i.e., the rank of the matrix gets much smaller than N_β). The number of time steps we must calculate $a(KT)$ is only $2N_\beta+1$. Nevertheless, the decay width can be accurately obtained even for states with lifetimes orders of magnitude longer than $2N_\beta+1$ [50].

Overlap probabilities $|d_j|^2$ together with the quasienergies and lifetimes for the Floquet states with the largest $|d_j|^2$ values are given in Table I. They largely control the long-time evolution of the wave packet. Note the very long lifetimes signifying quantum localization, which are only limited by the small direct photoionization rates. We find good agreement between Floquet states of the 3D Rydberg atom with $n_2^i=0$ and the 1D model. The energy distribution averaged over $\Delta E_0\approx 0.04$ for the 1D Floquet states is shown in Fig. 11. One intriguing result in Table I is that the lifetimes of the Floquet state No. 2 in 1D and in $n_2^i=0$ are about three orders of magnitude longer than the other ones. The spectral density in the continuum of this state is about three orders of magnitude smaller than that of the other ones, in clear correspondence to the long lifetime of the state. Similar results

TABLE I. Overlap probability to the initial state, real part of the quasienergies, and lifetimes for some Floquet states ($\nu_0=4$, $F_0^{av}=-0.02$, and $n_i=100$).

		$\lvert d_j\rvert^2$	$(\mathcal{E}_j^R)_0$	$(\tau_j)_0$
	1	0.368	-1.96×10^{-2}	5.9×10^{2}
1D	2	0.165	-1.11×10^{-2}	3.1×10^{5}
	3	0.148	-1.49×10^{-3}	8.0×10^{2}
	4	0.062	-1.51×10^{-2}	8.7×10^{2}
	5	0.049	-9.58×10^{-3}	2.4×10^{2}
	1	0.370	-1.93×10^{-2}	5.1×10^{2}
3D	2	0.163	-1.08×10^{-2}	3.3×10^{5}
$n_2^i=0$	3	0.145	-1.19×10^{-3}	6.1×10^{2}
	4	0.061	-1.47×10^{-2}	6.6×10^{2}
	5	0.051	-9.29×10^{-3}	2.2×10^{2}
	1	0.333	-1.40×10^{-2}	1.2×10^{3}
3D	2	0.144	-3.58×10^{-3}	9.5×10^{3}
$n_2^i=9$	3	0.114	-5.52×10^{-3}	9.4×10^{2}
	4	0.072	-4.17×10^{-3}	2.9×10^{3}
	5	0.055	-2.67×10^{-2}	4.4×10^{2}

hold for $n_2^i=0$. Note that the relative weight of a given Floquet state varies as $\lvert d_j\rvert^2\exp(-t/\tau_j)$, leading to a nonexponential decay of the system [51]. For 1D and $n_2^i=0$, state No. 1 dominates for times $K<2000$ relevant for experiments whereas for $K>2000$, state No. 2 dominates. This leads to a much smaller decay rate for very long times than seen in Fig. 5(a).

The energy distribution $\rho_0(E_0)$ and the distribution in the transverse degree of freedom $\rho_0((n_2)_0)$ for the Floquet states dominating at short times are shown in Fig. 12 for $n_2^i=0$ and $n_2^i=9$. Comparison with the distribution functions presented in Figs. 9 and 10 clearly shows the direct correspondence between the localized wave functions and the dominant Floquet states.

It is instructive to directly compare the spatial representation of the dominant Floquet states (Fig. 13) with the initial states (Fig. 2). While the overall extent in coordinate space remains unchanged the regular nodal pattern is destroyed due to the coherent superposition of a large number of unperturbed states for the eigenstates of this nonseparable problem.

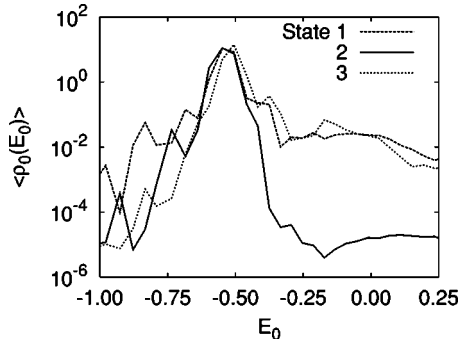

FIG. 11. Energy distributions averaged over $\Delta E_0\approx0.04$ for several Floquet states of the 1D model. The state labels correspond to those in Table I ($\nu_0=4$, $F_0^{av}=-0.02$, and $n_i=100$).

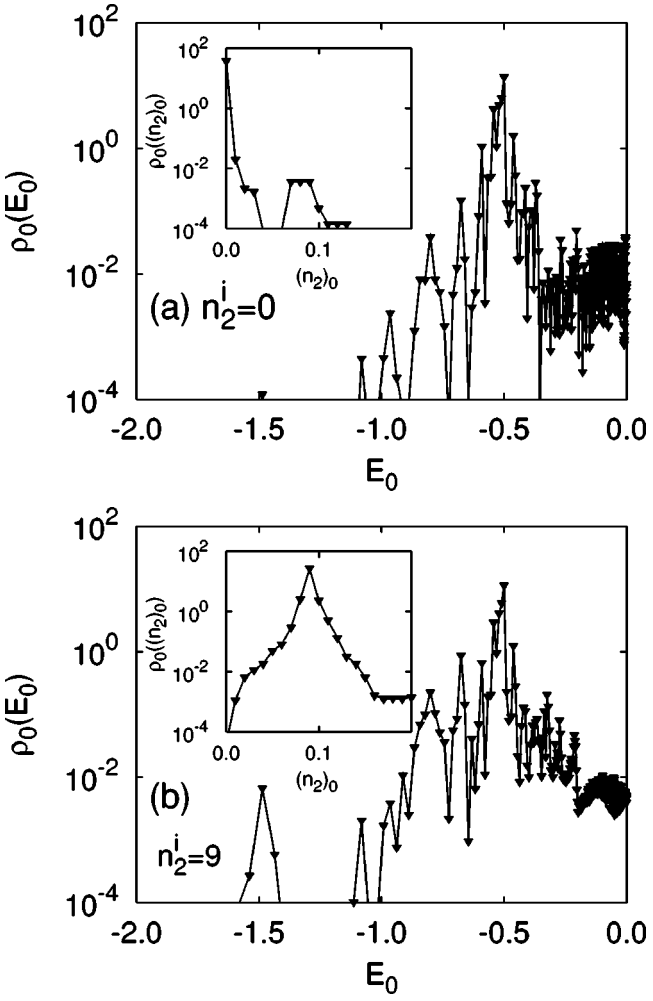

FIG. 12. Distributions in energy of the dominant Floquet state (number 1 in Table I) for (a) $n_2^i=0$ and (b) $n_2^i=9$. Insets: distributions in $(n_2)_0$ ($\nu_0=4$, $F_0^{av}=-0.02$, and $n_i=100$).

An alternative means to view quantum localization is the analysis of the phase space rather than the coordinate space representation of the Floquet states. We therefore calculate the Husimi phase-space distribution of the Floquet states. In Cartesian coordinates, it is defined as

$$W_H(\vec{r}_0,\vec{p}_0)=\left|\int d^3\vec{r}_0'\psi(\vec{r}_0')\varphi^*(\vec{r}_0',\vec{r}_0,\vec{p}_0)\right|^2, \quad (5.6)$$

where

$$\varphi(\vec{r}_0',\vec{r}_0,\vec{p}_0)=\sqrt{N}e^{-|\vec{r}_0-\vec{r}_0'|^2/2\alpha_0}e^{in_i\vec{r}_0'\cdot\vec{p}_0} \quad (5.7)$$

is a minimum-uncertainty Gaussian wave packet with normalization constant N. We proceed by transforming to cylindrical coordinates, $x=\rho\cos\phi$, $y=\rho\sin\phi$, and $z=z$. Due to the cylindrical symmetry of the wave function, the result is independent of ϕ. Setting $p_\phi=0$, we obtain the function $W_H(z_0,p_{z_0},\rho_0,p_{\rho_0})$ (see Ref. [52]). We choose the squeezing parameter $\alpha_0=\hbar_0=1/n_i$ such that the width is symmetric in scaled canonically conjugate coordinates (z_0,ρ_0) and mo-

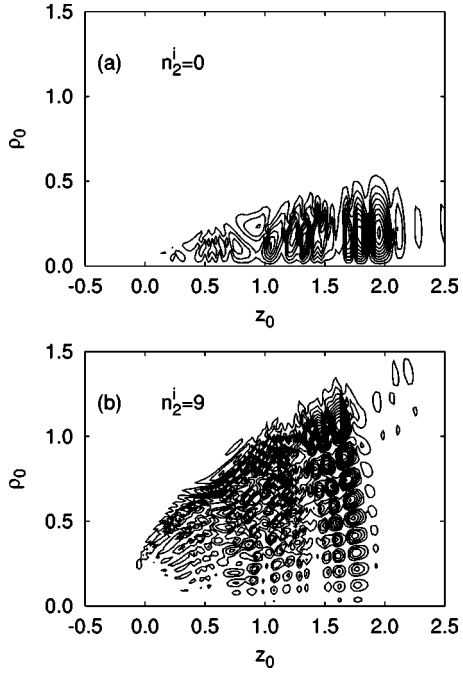

FIG. 13. Contour plots of the spatial probability density of the dominant Floquet states (state number 1 in Table I) for (a) $n_2^i=0$ and (b) $n_2^i=9$. ($\nu_0=4$, $F_0^{\mathrm{av}}=-0.02$, and $n_i=100$).

menta (p_{z_0},p_{ρ_0}). Consequently, the Gaussian wave packet has a width $1/\sqrt{n_i}$ in both z_0 and p_{z_0} and in ρ_0 and ρ_{p_0}.

The Husimi distribution of the 3D Rydberg atom describes a four-dimensional distribution which is difficult to visualize. We therefore view the cross section in two planes similar to classical Poincaré surfaces of section. We first consider the most elongated parabolic initial state with $n_2^i=0$. To emphasize the similarity to the 1D case, we cut the Husimi distribution at $\rho_0=p_{\rho_0}=0$ and calculate a cross section along the z_0 and p_{z_0} axes. We show contour plots of this cut together with the Husimi distribution for the 1D model in Figs. 14(a) and 14(b). The two distributions are practically identical and display clearly the localization in phase space in the vicinity of, but not coincident with, the initial hydrogenic torus. One of several [34,53] mechanisms responsible for quantum localization is the ''scarring'' of the Floquet states around unstable periodic orbits [12,35]. In the 1D case, it is easy to find the unstable periodic orbits (UPOs) [see Fig. 14(a)]. Note that the UPO which corresponds to the dominant Floquet state encircles the nucleus twice before returning to the same point in phase space. The Husimi distribution is localized near the classical unstable fixed points. The size of the distribution around the fixed points is in the order of $\hbar_0$. (The area $\hbar_0$ is indicated by the size of the box).

The same UPO exists also in the 3D case, namely, in the limit $\rho_0\rightarrow 0$ and $p_{\rho_0}\rightarrow 0$, and is depicted in Fig. 14(b). We also show in Fig. 14(c) a cut along the $\rho_0-p_{\rho_0}$ plane taken at $z_0=1.9$ and $p_{z_0}=-0.2$, which corresponds to a peak in Fig. 14(b). The figure illustrates that the Husimi distribution in the ρ_0 and p_{ρ_0} plane is concentrated near $\rho_0=p_{\rho_0}=0$. Taking into account the uncertainty in ρ_0 and p_{ρ_0} (indicated

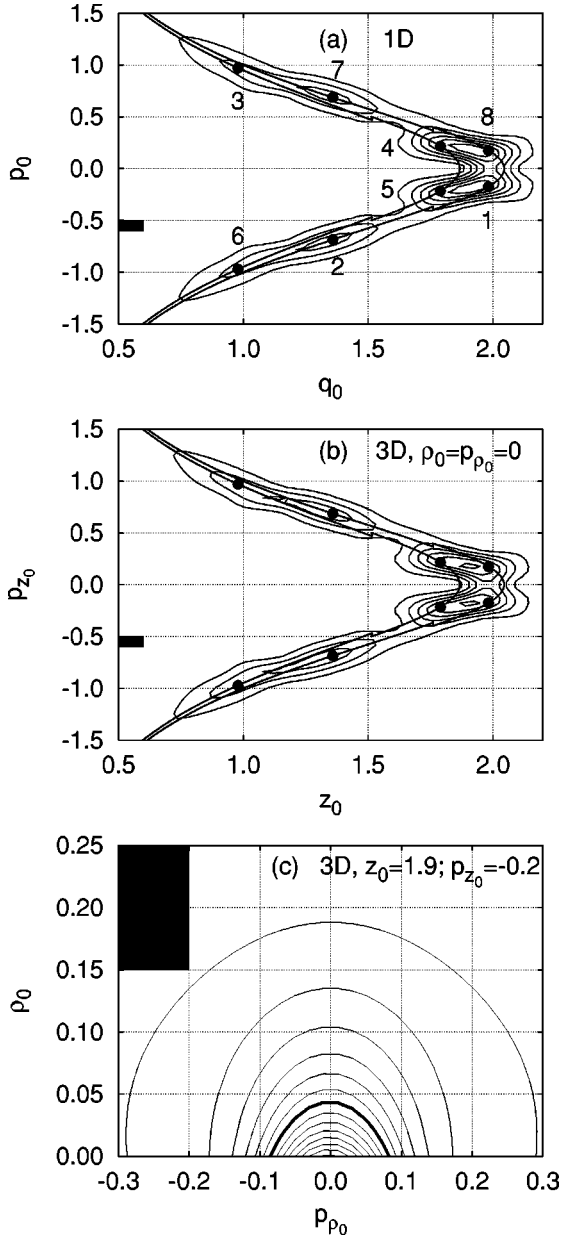

FIG. 14. Contour plots of the Husimi distributions of the dominant Floquet states (state number 1 in Table I) for (a) the 1D kicked atom and (b, c) different cuts in the 3D case with $n_2^i=0$ ($\nu_0=4$, $F_0^{\mathrm{av}}=-0.02$, and $n_i=100$). The boxes indicate in each case the size of $\hbar_0$. In (a) and (b), the points denote the unstable fix points of the corresponding unstable periodic orbit (UPO). The numbers in (a) indicate the time ordering within which the fix points are visited. The thick line in (c) denotes the contour for half of the maximum value.

by the box), we can interpret the structures seen in the full 3D Husimi distribution for $n_2^i=0$ as being caused by ''scarring'' around the UPO at $\rho_0=p_{\rho_0}=0$ already found in 1D. We are thus able to verify that the Floquet states in the 3D case for the most elongated initial state ($n_2^i=0$) localize in phase space around the UPOs.

An interesting question is whether the ''scarring'' of the Husimi distribution around the UPO exists also for the less

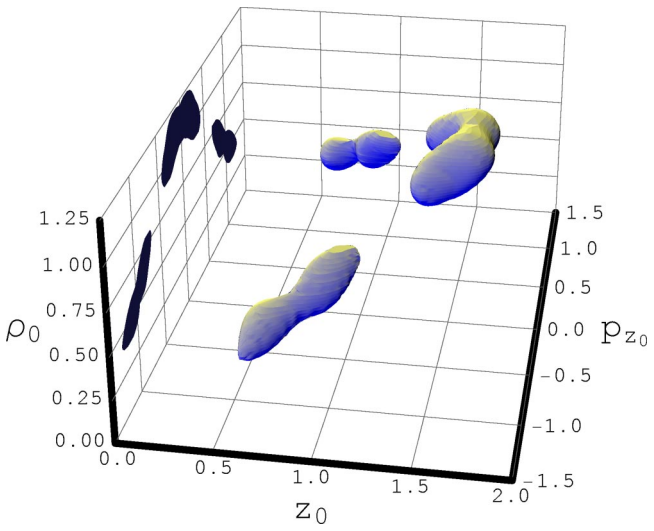

FIG. 15. (Color online) Three-dimensional representation of the Husimi distribution integrated over p_{ρ_0} of the dominant Floquet state (number 1 in Table I) for $n_2^i=9$. We show the contour surface taken at 1/4 of the maximum value. Projection of the data onto the surface $z_0=0$ is indicated ($\nu_0=4$, $F_0^{\mathrm{av}}=-0.02$, and $n_i=100$).

elongated initial state with $n_2^i=9$, which explores the four-dimensional phase space. Since it is difficult to display the 4D Husimi distribution, we display in Fig. 15 a three-dimensional Husimi distribution obtained by integrating over p_ρ. Specifically, we show the surface taken at 1/4 of the maximum value. Note that the Husimi distribution is localized close to the plane with $\tan\rho/z=36°$, where also the initial state was situated. The localization observed in Fig. 15 is most likely due to unstable fixed points of UPOs exploring the 4D phase space. So far, we have not succeeded in identifying the relevant UPOs but leave this challenging task for future studies.

VI. CONCLUSIONS AND OUTLOOK

We have shown that quantum localization takes place in the three-dimensional kicked Rydberg atom. The quantum survival and recurrence probabilities are significantly larger than the classical values and the quantum diffusion both along the energy axis and the parabolic quantum number n_2 is suppressed. We have demonstrated localization for two different initial states: (a) the most elongated parabolic state for which we find close similarities to the earlier studied 1D model and (b) a less elongated parabolic state with $\langle\cos\theta\rangle \approx 0.8$, i.e., where already the initial state explores the full 3D dynamics. To our knowledge, this is the first detailed verification of quantum localization in the 3D kicked Rydberg atom.

We were able to extract the relevant Floquet states, i.e., eigenstates of the period-one time-evolution operator, for the 3D kicked Rydberg atom by harmonic inversion. Localized Floquet states directly correspond to the quantum localization observed in the time-dependent wave function. The Husimi distributions of the Floquet states are localized in phase space both for the most elongated initial state as well as for less elongated initial states. For the most elongated parabolic initial state, the Husimi distribution localizes around the same unstable periodic orbits as in the corresponding 1D case.

Our analysis predicts that quantum localization should be observable in the survival probabilities for frequencies as low as $\nu_0 \approx 4$ and average field $F_0^{\mathrm{av}} \approx -0.02$ within 200 to 300 kicks at $n_i \approx 350$ if the Rydberg atom is initially prepared in an elongated parabolic state. This quantum effect should appear after a time of $t \gtrsim 50 T_n$, which is earlier than the time for the first full revival of a wave packet after subjecting the atom to a single ultrashort half-cycle pulse expected at $t_n \geqslant (n/3) T_n \approx 110 T_n$ [36], thus posing a less stringent requirement on quantum phase coherence in the experiment. Clearly, quantum localization in the recurrence probability would be observable at even much shorter time scales, as would partial revivals. The recurrence would, in turn, require a more sophisticated detection scheme such as resonant ionization of the recurrent initial state. On the theoretical side, identification of unstable periodic orbits that explore the full 4D phase space and are responsible for scarring in higher dimensions remains a challenging task.

ACKNOWLEDGMENTS

This work was supported by the FWF (Austria) under Contract No. SFB-016. C.R. acknowledges support by U.S. DOE OBES, DCS managed by UT-Battelle, LLC.

[1] M. C. Gutzwiller, *Chaos in Classical and Quantum Mechanics* (Springer-Verlag, New York, 1990).
[2] H.-J. Stöckmann, *Quantum Chaos, an Introduction* (Cambridge University Press, Cambridge, England, 1999).
[3] G. Casati, B.V. Chirikov, D.L. Shepelyansky, and I. Guarneri, Phys. Rep. **154**, 77 (1987); G. Casati, I. Guarneri, and D.L. Shepelyansky, IEEE J. Quantum Electron. **24**, 1420 (1988).
[4] G. Casati, B.V. Chirikov, F.M. Izraelev, and J. Ford, Lect. Notes Phys. **93**, 334 (1979); G. Casati, I. Guarneri, and D.L. Shepelyansky, Phys. Rev. Lett. **62**, 345 (1989).
[5] S. Fishman, D.R. Grempel, and R.E. Prange, Phys. Rev. Lett. **49**, 509 (1982); D.R. Grempel, R.E. Prange, and S. Fishman, Phys. Rev. A **29**, 1639 (1984); E. Doron and S. Fishman, Phys. Rev. Lett. **60**, 867 (1988).
[6] B. Georgeot and D.L. Shepelyansky, Phys. Rev. Lett. **86**, 2890 (2001).
[7] S. Adachi, M. Toda, and K. Ikeda, Phys. Rev. Lett. **61**, 659 (1988).
[8] F.L. Moore, J.C. Robinson, C.F. Bharucha, B. Sundaram, and M.G. Raizen, Phys. Rev. Lett. **75**, 4598 (1995).
[9] J.E. Bayfield and L.A. Pinnaduwage, Phys. Rev. Lett. **54**, 313 (1985).
[10] P.M. Koch and K.A.H. van Leeuwen, Phys. Rep. **255**, 289 (1995).

[11] A. Buchleitner, I. Guarneri, and J. Zakrzewski, Europhys. Lett. **44**, 162 (1998); S. Wimberger and A. Buchleitner, J. Phys. A **34**, 7181 (2001).
[12] R.V. Jensen, S.M. Susskind, and M.M. Sanders, Phys. Rep. **201**, 1 (1991).
[13] J. Leopold and D. Richards, J. Phys. B **22**, 1931 (1989).
[14] A. Buchleitner and D. Delande, Chaos, Solitons Fractals **5**, 1125 (1995).
[15] A. Buchleitner and D. Delande, Phys. Rev. Lett. **70**, 33 (1993).
[16] R. R Jones, D. You, and P.H. Bucksbaum, Phys. Rev. Lett. **70**, 1236 (1993).
[17] M.T. Frey, F.B. Dunning, C.O. Reinhold, and J. Burgdörfer, Phys. Rev. A **53**, R2929 (1996).
[18] J. Bromage and C.R. Stroud, Phys. Rev. Lett. **83**, 4963 (1999).
[19] A. Dhar, M. Nagaranjan, F. Izrailev, and R. Whitehead, J. Phys. B **16**, L17 (1983); A. Carnegie, *ibid.* **17**, 3435 (1984).
[20] R. Blümel and U. Smilansky, Phys. Rev. A **30**, 1040 (1984).
[21] J. Burgdörfer, Nucl. Instrum. Methods Phys. Res. B **42**, 500 (1989); M. Melles, C.O. Reinhold, and J. Burgdörfer, *ibid.* **79**, 109 (1993).
[22] C.F. Hillermeier, R. Blümel, and U. Smilansky, Phys. Rev. A **45**, 3486 (1992).
[23] G. Casati, I. Guarneri, and G. Mantica, Phys. Rev. A **50**, 5018 (1994); H. Wiedemann, J. Mostowski, and F. Haake, *ibid.* **49**, 1171 (1994).
[24] C.O. Reinhold, M. Melles, and J. Burgdörfer, Phys. Rev. Lett. **70**, 4026 (1993).
[25] C.O. Reinhold, J. Burgdörfer, M.T. Frey, and F.B. Dunning, Phys. Rev. Lett. **79**, 5226 (1997).
[26] M. Klews and W. Schweizer, Phys. Rev. A **64**, 053403 (2001).
[27] J. Ahn, D.N. Hutchinson, C. Rangan, and P.H. Bucksbaum, Phys. Rev. Lett. **86**, 1179 (2001); T.J. Bensky, M.B. Campbell, and R.R. Jones, *ibid.* **81**, 3112 (1998).
[28] C. Wesdorp, F. Robicheaux, and L.D. Noordam, Phys. Rev. Lett. **87**, 083001 (2001); C. Wesdorp, F. Robicheaux, and L.D. Noordam, Phys. Rev. A **60**, 5122 (1999).
[29] E. Persson, S. Yoshida, X.M. Tong, C.O. Reinhold, and J. Burgdörfer, Phys. Rev. A **66**, 043407 (2002).
[30] M.T. Frey, F.B. Dunning, C.O. Reinhold, S. Yoshida, and J. Burgdörfer, Phys. Rev. A **59**, 1434 (1999).
[31] M.V. Berry, Physica D **33**, 26 (1988).
[32] P.W. Anderson, Phys. Rev. **109**, 1492 (1958); Rev. Mod. Phys. **50**, 191 (1978).
[33] D.J. Thouless, Phys. Rep. **13**, 93 (1974); E. Abrahams, P.W. Anderson, D.C. Licciardello, and T.V. Ramakrishnan, Phys. Rev. Lett. **42**, 673 (1979).
[34] D. Bensimon and L. Kadanoff, Physica D **13**, 82 (1984); R.S. Mackay, J.D. Meiss, and I.C. Percival, *ibid.* **13**, 55 (1984).
[35] S. Yoshida, C.O. Reinhold, and J. Burgdörfer, Phys. Rev. Lett. **84**, 2602 (2000); S. Yoshida, C.O. Reinhold, P. Kristöfel, and J. Burgdörfer, Phys. Rev. A **62**, 023408 (2000).
[36] J. Parker and C.R. Stroud, Phys. Rev. Lett. **56**, 716 (1986); J.A. Yeazell and C.R. Stroud, *ibid.* **60**, 1494 (1988); Z.D. Gaeta and C.R. Stroud, Phys. Rev. A **42**, 6308 (1990).
[37] B.E. Tannian, C.L. Stokely, F.B. Dunning, C.O. Reinhold, S. Yoshida, and J. Burgdörfer, Phys. Rev. A **62**, 043402 (2000).
[38] C.O. Reinhold, M. Melles, H. Shao, and J. Burgdörfer, J. Phys. B **26**, L659 (1993).
[39] X.M. Tong and S.I. Chu, Chem. Phys. **217**, 119 (1997); J. Wang, S.I. Chu, and C. Laughlin, Phys. Rev. A **50**, 3208 (1994).
[40] I. Bersons and A. Kulsh, Phys. Rev. A **55**, 1674 (1997).
[41] S. Yoshida, S. Watanabe, C.O. Reinhold, and J. Burgdörfer, Phys. Rev. A **60**, 1113 (1999).
[42] Multiplying the masking function Eq. (2.19) after each kick yields convergence for high kick frequencies. For frequencies considerably lower than that used in this work, the free evolution should be split into partial free evolution operators and the wave function multiplied by the masking function after each partial time evolution.
[43] A. Buchleitner and D. Delande, Phys. Rev. A **55**, R1585 (1997).
[44] J.G. Leopold and D. Richards, J. Phys. B **20**, 2369 (1987).
[45] C.O. Reinhold and J. Burgdörfer, Phys. Rev. A **51**, R3410 (1995).
[46] H. A. Bethe and E. Salpeter, *Quantum Mechanics of One-and Two-Electron Atoms* (Plenum, New York, 1977).
[47] M. J. Englefield, *Group Theory of the Coulomb Problem* (Wiley-Interscience, New York, 1972).
[48] C. L. Stokely, J. C. Lancaster, F. B. Dunning, D. G. Arbó, C. O. Reinhold, and J. Burgdörfer, Phys. Rev. A **67**, 013403 (2003).
[49] A. Maquet, Shih-I chu, and W.P. Reinhardt, Phys. Rev. A **27**, 2946 (1983); C.R. Holt, M.G. Raymer, and W.P. Reinhardt, *ibid.* **27**, 2971 (1983).
[50] V.A. Mandelshtam and H.S. Taylor, J. Chem. Phys. **107**, 6756 (1997).
[51] A. Buchleitner, D. Delande, J. Zakrzewski, R.N. Mantegna, M. Arndt, and H. Walther, Phys. Rev. Lett. **75**, 3818 (1995).
[52] The function $W_H(z_0, p_{z_0}, \rho_0, p_{\rho_0})$ is given by $|2\pi\int \rho_0' d\rho_0' dz' \psi(z_0', \rho_0')\varphi^* F|^2$ with $\varphi = \sqrt{N}\exp\{-[(z_0'-z_0)^2 + (\rho_0'-\rho_0)^2]/2\alpha_0\}\exp[in_i(z_0' p_{z_0} + \rho_0' p_{\rho_0})]$ and $F = 2\pi \exp(-\rho_0'\rho_0/\alpha_0) I_0(\rho_0'\rho_0/\alpha_0 + in_i\rho_0' p_{\rho_0})$ with I a modified Bessel function.
[53] F. Grossman *et al.* (unpublished).